

# Van der Waals epitaxy of tunable moirés enabled by alloying

Received: 9 November 2022

Accepted: 31 May 2023

Published online: 14 August 2023



Matthieu Fortin-Deschênes<sup>1</sup>✉, Kenji Watanabe<sup>2</sup>, Takashi Taniguchi<sup>3</sup>  
& Fengnian Xia<sup>1</sup>✉

The unique physics in moiré superlattices of twisted or lattice-mismatched atomic layers holds great promise for future quantum technologies. However, twisted configurations are thermodynamically unfavourable, making accurate twist angle control during growth implausible. While rotationally aligned, lattice-mismatched moirés such as WSe<sub>2</sub>/WS<sub>2</sub> can be synthesized, they lack the critical moiré period tunability, and their formation mechanisms are not well understood. Here, we report the thermodynamically driven van der Waals epitaxy of moirés with a tunable period from 10 to 45 nanometres, using lattice mismatch engineering in two WSe layers with adjustable chalcogen ratios. Contrary to conventional epitaxy, where lattice-mismatch-induced stress hinders high-quality growth, we reveal the key role of bulk stress in moiré formation and its unique interplay with edge stress in shaping the moiré growth modes. Moreover, the superlattices display tunable interlayer excitons and moiré intralayer excitons. Our studies unveil the epitaxial science of moiré synthesis and lay the foundations for moiré-based technologies.

Overlaying the lattices of two-dimensional (2D) materials with a twist angle or lattice mismatch generates a larger (quasi-) periodic moiré pattern<sup>1–4</sup>. The moiré drastically influences the properties of van der Waals (vdW) heterostructures (HSs) due to the formation of a long-periodicity potential and the emergence of additional moiré electronic bands. In moiré transition metal dichalcogenides (TMDs), there exist intralayer and interlayer exciton minibands as well as moiré trapped excitons<sup>5–10</sup>. In ‘magic-angle’ twisted bilayer graphene, the minimized electron kinetic energy in the moiré flat bands leads to strongly correlated phases such as unconventional superconductivity and ferromagnetism<sup>11–14</sup>. The unique physics in moiré materials therefore holds substantial potential for the development of innovative technologies<sup>9,15–17</sup>. Experimentally, moiré HSs are usually fabricated by stacking mechanically exfoliated layers with a precisely controlled twist angle<sup>3</sup> or by rotationally aligning lattice-mismatched layers<sup>5,6,10</sup>. The accurate rotational misalignment allows one to finely tune the properties of the HSs. Nonetheless, this method suffers from important limitations such as the introduction of interlayer contamination. More importantly,

exfoliation is inherently not scalable, which hinders the use of moiré materials in emerging quantum technologies.

Large-scale synthesis can overcome the fundamental limitations of mechanical exfoliation<sup>18</sup>. While the vdW epitaxy of twisted moiré graphene has been demonstrated<sup>19,20</sup>, accurate twist angle control is very challenging, since twisted configurations are almost all equally thermodynamically unfavourable. Furthermore, twisted bilayer graphene was recently synthesized by etching Cu/twisted bilayer graphene/Cu sandwich structures obtained by growing monolayer graphene on two prerotated monocrystalline Cu foils<sup>21</sup>. Rotationally aligned moirés including graphene/hexagonal boron nitride (hBN) and TMDs have also been grown by vdW epitaxy<sup>22–34</sup>. Despite this progress, foundational issues for moiré vdW epitaxy, such as the mechanisms and conditions for moiré formation, have not yet been addressed. More importantly, in these earlier studies, the period of rotationally aligned moirés lacks the critical tunability and is restricted to a handful of discrete values determined by the layers’ lattice parameters. For these reasons, the synthesis of two aligned atomic layers with

<sup>1</sup>Department of Electrical Engineering, Yale University, New Haven, CT, USA. <sup>2</sup>Research Center for Functional Materials, National Institute for Materials Science, Tsukuba, Japan. <sup>3</sup>International Center for Materials Nanoarchitectonics, National Institute for Materials Science, Tsukuba, Japan.  
✉e-mail: [matthieu.fortin-deschenes@yale.edu](mailto:matthieu.fortin-deschenes@yale.edu); [fengnian.xia@yale.edu](mailto:fengnian.xia@yale.edu)

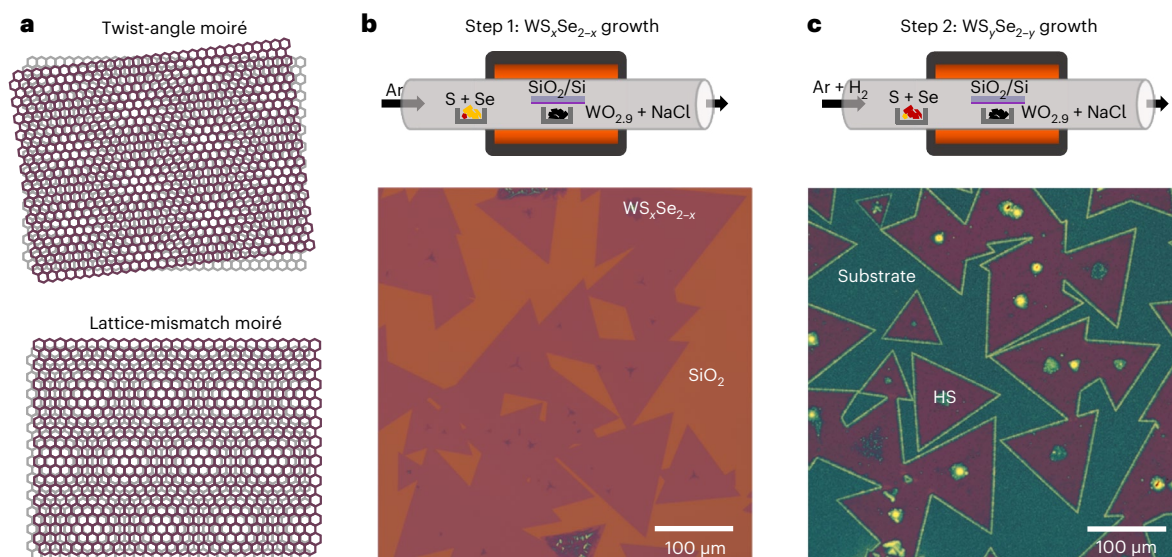


**Fig. 1 | Growth of moiré vdW heterostructures.** **a**, Schematics of moirés resulting from a twist between two 2D layers (top) and the stacking of lattice-mismatched layers (bottom). The twist angle and the magnitude of the lattice mismatch determine the moiré periods in these two cases, respectively. **b**, First step of the two-step CVD growth process of WS<sub>y</sub>Se<sub>2-y</sub>/WS<sub>x</sub>Se<sub>2-x</sub>. During this step,

monolayer WS<sub>x</sub>Se<sub>2-x</sub> flakes are grown on SiO<sub>2</sub>/Si, as seen in the optical micrograph at the bottom. **c**, Second step of the vdW HS growth process. In this step, WS<sub>y</sub>Se<sub>2-y</sub> is grown on WS<sub>x</sub>Se<sub>2-x</sub>. The darker purple triangular flakes in the optical micrograph (bottom) are the WS<sub>y</sub>Se<sub>2-y</sub>/WS<sub>x</sub>Se<sub>2-x</sub> vdW HSS. The teal regions are multilayer WS<sub>y</sub>Se<sub>2-y</sub> on SiO<sub>2</sub>.

controllable lattice mismatch represents a promising strategy for realizing large-scale stable moirés with tunable periodicity (Fig. 1a). In fact, in most 2D materials, interchanging elements within a group of the periodic table, especially in the *p*-block, allows one to change the lattice constant while minimally modifying the electronic band structure.

Herein, using TMDCs as a model system, we demonstrate that substitutional alloying allows one to continuously tune the moiré period of vdW HSS using a thermodynamically driven growth process. We grow WS<sub>y</sub>Se<sub>2-y</sub>/WS<sub>x</sub>Se<sub>2-x</sub> vdW HSS with different sulfur/selenium ratios using chemical vapour deposition (CVD) and obtain moirés with a tunable period of 10–45 nm. We then elucidate the moiré formation mechanisms and reveal the unique growth modes based on transmission electron microscopy measurements and modelling of the moiré nuclei. Finally, by examining the photoluminescence (PL) of the vdW HSS, we demonstrate the tunability of the interlayer exciton and the presence of intralayer moiré excitons. Our work identifies the key mechanisms driving moiré formation and provides a pathway for the integration of tunable, thermodynamically stable moiré semiconductor materials in future quantum technologies.

## Growth of vdW HSS with tunable moiré

Moiré HSS were grown on 300 nm SiO<sub>2</sub>/Si substrates using a two-step CVD process, illustrated in Fig. 1b,c. First, sulfur-rich monolayer WS<sub>x</sub>Se<sub>2-x</sub> was grown using S, Se and WO<sub>2.9</sub>/NaCl precursors, with Ar carrier gas, as shown in Fig. 1b (details in Methods). WS<sub>x</sub>Se<sub>2-x</sub> mostly grows as monolayer triangular flakes with a size of 50–200 μm, as shown in Fig. 1b and Supplementary Figs. 1–3. In the second step, a selenium-rich WS<sub>y</sub>Se<sub>2-y</sub> monolayer was grown on WS<sub>x</sub>Se<sub>2-x</sub> using Ar + H<sub>2</sub> carrier gas and a larger Se/S ratio (Fig. 1c). The ratio of the Se/S precursors controls the composition. WS<sub>y</sub>Se<sub>2-y</sub> usually forms a continuous monolayer on the WS<sub>x</sub>Se<sub>2-x</sub> flakes, creating WS<sub>y</sub>Se<sub>2-y</sub>/WS<sub>x</sub>Se<sub>2-x</sub> vertical vdW HSS, as seen in the optical micrograph in Fig. 1c and in the atomic force microscopy images in Supplementary Fig. 2. We note that multilayer WS<sub>y</sub>Se<sub>2-y</sub> grows at the edges and on the central nuclei of the WS<sub>x</sub>Se<sub>2-x</sub> triangular flakes, as well as on SiO<sub>2</sub> (teal layer in Fig. 1c). Moreover, WS<sub>y</sub>Se<sub>2-y</sub> grows in a quasi-layer-by-layer fashion on monolayer WS<sub>x</sub>Se<sub>2-x</sub> (Supplementary Fig. 4). Partial growth experiments suggest that WS<sub>y</sub>Se<sub>2-y</sub> is formed from coalesced, rotationally aligned (2H and 3R) domains with a lateral size

of up to 10 μm (Supplementary Fig. 4). While not studied in detail in this work, controlling the nucleation may allow one to grow pure 2H or 3R domains (Supplementary Fig. 5)<sup>26,35–39</sup>.

Next, we look at the atomic structure of the vdW HSS using (scanning) transmission electron microscopy (S/TEM). Fig. 2b shows a STEM image of a moiré unit cell of the WS<sub>0.35</sub>Se<sub>1.65</sub>/WS<sub>1.88</sub>Se<sub>0.12</sub> sample that is shown in Fig. 2a. The two layers are rotationally aligned but have different lattice parameters (3.16 Å and 3.26 Å), as evidenced by the two hexagonal sets of spots in the fast Fourier transform (FFT) of the large-scale transmission electron microscopy (TEM) image (yellow squares in Fig. 2c). Moreover, the intensity of the two sets of spots, both in the FFT (Fig. 2c) and diffraction pattern (Supplementary Fig. 6), is comparable. This indicates that the two layers have the same thickness (that is, monolayers), in agreement with the measurements in Fig. 2a and Supplementary Fig. 2. The smaller hexagonal pattern (magenta squares in Fig. 2c) originates from a large-scale moiré with a 10.4 nm lattice constant. Furthermore, the atomic and moiré reciprocal lattices are aligned within 1°, as measured from the FFT in Fig. 2c. This implies that the two layers are aligned within ~0.03°, as discussed in the next sections.

The effectiveness of moiré compositional tuning is assessed by comparing vdW HSS grown under different Se/S ratios. The compositions of the HSS are determined using energy-dispersive X-ray spectroscopy, as shown in Supplementary Fig. 7 (details in Methods). The selenium content difference between the two WS<sub>y</sub>Se<sub>2-y</sub>/WS<sub>x</sub>Se<sub>2-x</sub> layers, defined as  $\Delta\text{Se} = (x - y)/2$ , ranges from 17–77%, and moiré patterns are formed in every sample. The periodicity of relaxed moirés increases from 10 to 45 nm when  $\Delta\text{Se}$  decreases from 77% to 17%, as illustrated in Fig. 2d, due to the narrowing equilibrium lattice mismatch ( $\Delta a$ ). The expected relaxed moiré lattice parameter is

$$a_{\text{moiré}} = \frac{a_{\text{WS}_x\text{Se}_{2-x}} a_{\text{WS}_y\text{Se}_{2-y}}}{(a_{\text{WS}_y\text{Se}_{2-y}} - a_{\text{WS}_x\text{Se}_{2-x}})} \approx \frac{a_{\text{WSSe}}^2}{\Delta\text{Se} (a_{\text{WSe}_2} - a_{\text{WS}_2})} \quad (1)$$

where  $a_{\text{WS}_{x(y)}\text{Se}_{2-x(y)}}$  is the lattice constant of monolayer WS<sub>x(y)</sub>Se<sub>2-x(y)</sub>. The measurements agree with the calculated moiré periodicity based on equation (1) as illustrated in Fig. 2e, indicating that the two layers

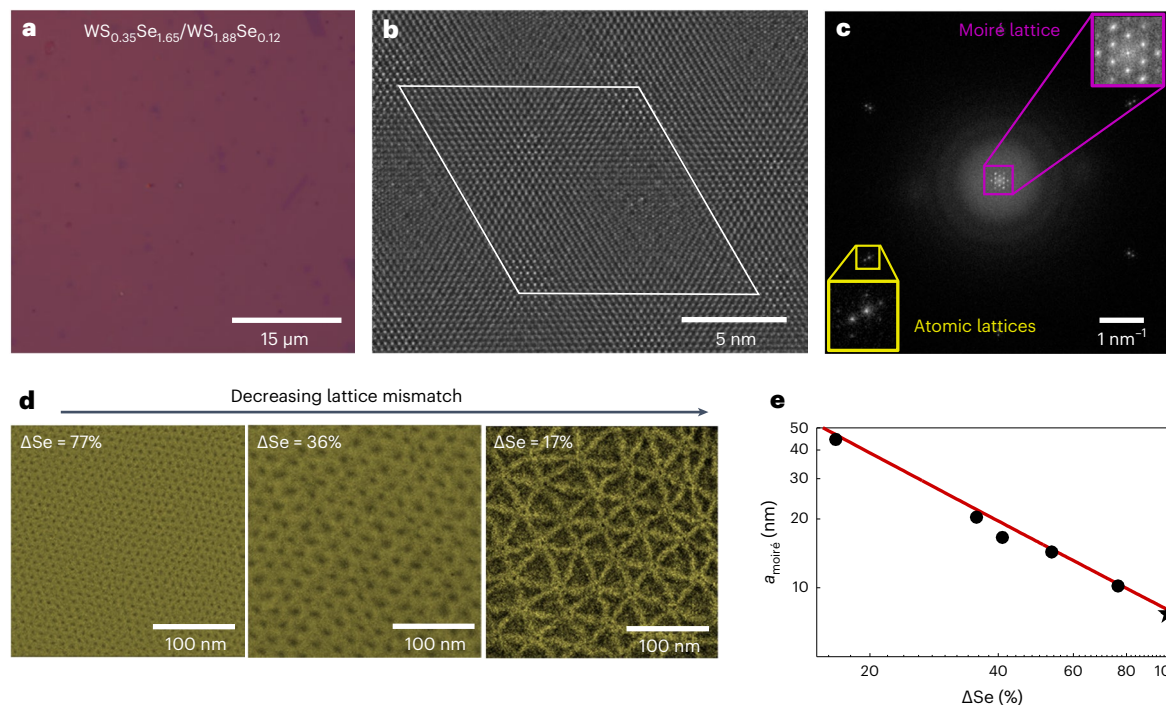


**Fig. 2 | Tunable moiré pattern in  $WS_xSe_{2-y}/WS_xSe_{2-x}$  vdW HSs.** **a**, Optical micrograph of a  $WS_{0.35}Se_{1.65}/WS_{1.88}Se_{0.12}$  vdW HS. The composition is determined by energy-dispersive X-ray spectroscopy. **b**, High-magnification STEM micrograph of the moiré unit cell of the  $WS_{0.35}Se_{1.65}/WS_{1.88}Se_{0.12}$  sample in **a**. **c**, FFT of a large-area TEM image of the sample shown in **a** and **b**. The yellow and magenta squares show the atomic and moiré reciprocal lattices, respectively. Enlarged images of these regions are shown in the bottom left and top right.

**d**, False-coloured TEM micrographs of the moirés of relaxed vdW HSs with different compositions and moiré periodicities. The moiré pattern observed for  $\Delta Se = 17\%$  (dark triangles) results from atomic reconstructions that create domain boundaries, similar to those seen in small-angle twisted bilayers<sup>58</sup>, as detailed in Supplementary Fig. 8. **e**, Composition dependence of the lattice constant of relaxed moirés. The filled circles are samples grown in this work, and the star is the measured moiré period of  $WSe_2/WS_2$  from the literature<sup>31</sup>.

are relaxed to their equilibrium lattice constant. However, for small  $\Delta a$  ( $\Delta Se = 17\%$ ), partial relaxation and larger moiré periodicities are observed in some regions, as discussed in the next sections.

## Stress relaxation and moiré formation mechanisms

To better understand moiré formation, we look at the nucleation and stress relaxation mechanisms. Below, we consider the energy landscape of small, rotationally aligned  $WS_ySe_{2-y}$  nuclei on continuous  $WS_xSe_{2-x}$  during the second growth step. The lattice-mismatch-induced strain is assumed to be localized only in the top layer nuclei since the continuity of the bottom  $WS_xSe_{2-x}$  layer and its interaction with the growth substrate restrict local deformations. However, small nuclei can expand and contract by slipping at their edges. The energy difference per unit area ( $\Delta E$ ) between relaxed and lattice-matched (epitaxial) nuclei can be understood as

$$\Delta E = \Delta E_{\text{int}} + \Delta U_{\text{bulk}} + \Delta U_{\text{edges}}. \quad (2)$$

Here, the first two terms on the right-hand side are the change in the interlayer interaction energy ( $\Delta E_{\text{int}}$ ) and bulk strain energy ( $\Delta U_{\text{bulk}}$ ), when leaving the epitaxial configuration. On the other hand, the edge strain energy term ( $\Delta U_{\text{edges}}$ ) is distinct from  $\Delta U_{\text{bulk}}$  since the equilibrium interatomic distances at the edges of the nuclei are modified due to dangling bonds. The edge stress ( $\tau_{\text{edges}}$ ) is expected to be tensile for TMDCs<sup>40</sup>.

We highlight the importance of the three terms in equation (2) by estimating the energy of triangular nuclei as a function of their lattice constant. The large system size prevents the use of density functional theory to evaluate equation (2). We therefore use an interatomic potential consisting of intralayer bonded interactions and interlayer vdW

and ionic interactions (details in Supplementary Fig. 9 and Methods)<sup>41</sup>. Since there are no experimentally validated interatomic potentials for  $WS_xSe_{2-x}$ , we use an accurate model validated for  $MoS_2$  (ref. 41). In our model, the lattice mismatch between the two layers in their respective equilibrium state ( $\Delta a$ ) is modelled by modifying the lattice parameter of the bottom layer and fixing its atomic structure (details in Methods). Edge stress is introduced by shortening the equilibrium bond length at the nuclei's edges. The three contributions to the energy can be directly separated and are plotted as a function of the top nuclei's lattice parameter in Fig. 3a,b for nuclei with  $\Delta a$  of 0.052 Å and side length ( $L$ ) values of 13 nm and 153 nm, respectively. The bulk strain energy ( $U_{\text{bulk}}$ ) favours the relaxed configuration, and the interlayer interaction energy ( $E_{\text{int}}$ ) favours the lattice-matched state (Fig. 3a,b). The value of  $U_{\text{bulk}}$  is independent from  $L$ , but  $E_{\text{int}}$  narrows as  $L$  increases since the average atomic displacement from the lattice-matched sites, resulting from the nuclei's expansion or contraction, scales with  $L$ . On the other hand, the tensile edge strain energy per unit area ( $U_{\text{edges}}$ ) scales as  $1/L$  and favours compression of the nuclei (Fig. 3a,b). The relative magnitudes and signs of these three energy terms fundamentally shape the moiré growth modes, as discussed in the following.

The evolution of the energy versus lattice constant for top  $WS_ySe_{2-y}$  nuclei of increasing  $L$  is shown in Fig. 3c,d for vdW HSs with  $\Delta a$  values of 0.034 Å and 0.052 Å, respectively. Due to the broad nature of  $E_{\text{int}}$  in small nuclei, the  $E_{\text{int}}$  and  $U_{\text{bulk}}$  minima merge for small  $L$ , as illustrated in Fig. 3c,d. We suggest that the path followed by the nuclei to minimize their energy as the two minima separate during growth (arrows in Fig. 3c,d) dictates the moiré growth modes, which are illustrated in Fig. 3c,d (insets) and Fig. 3e–g. When  $-\frac{\Delta U_{\text{bulk}}}{\Delta E_{\text{int}}} < 1$ , the lattice-matched configuration is favoured and epitaxial growth of strained vdW HSs is expected, as illustrated by the striped region in Fig. 3e. However, if  $\Delta a$



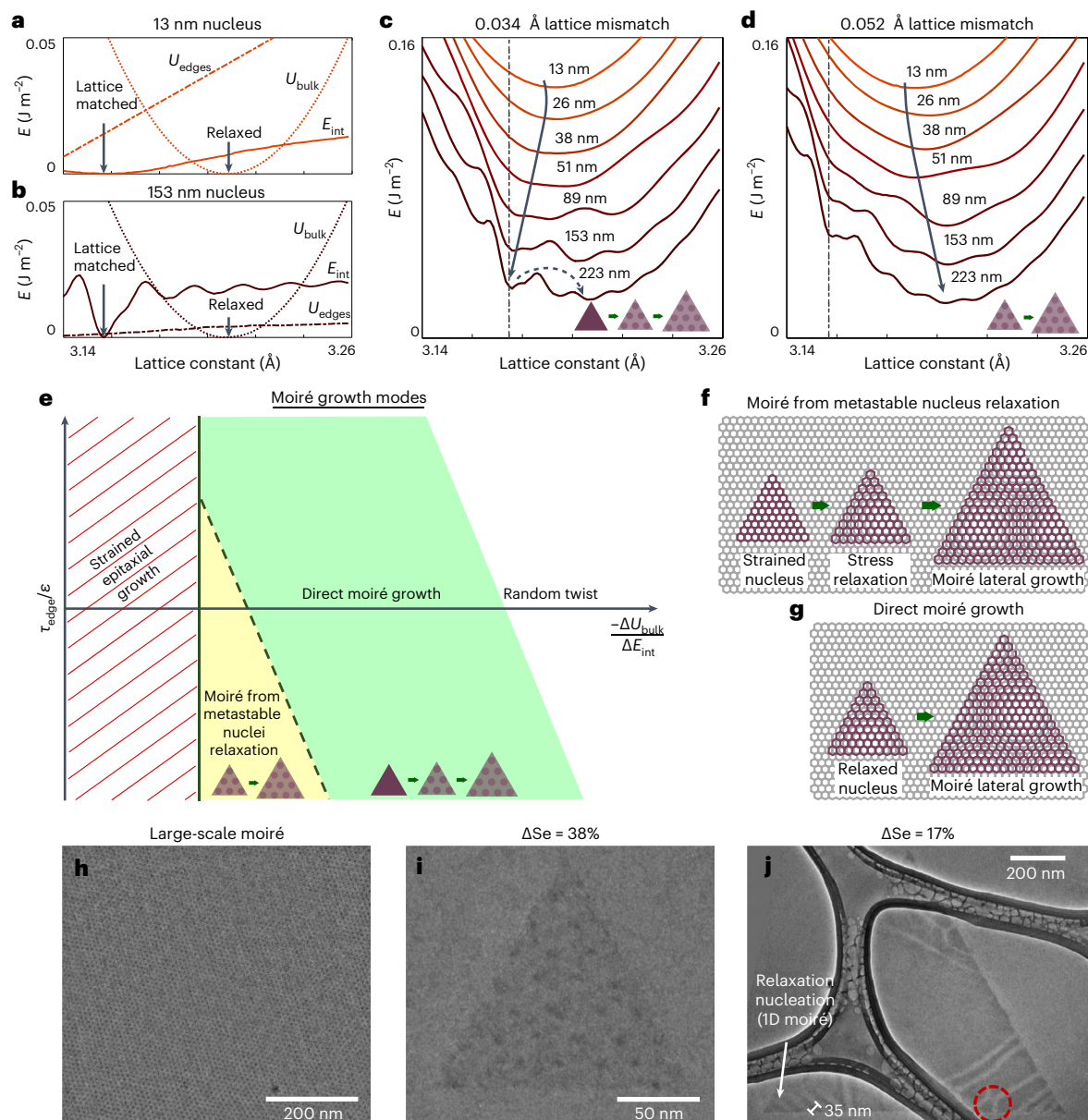


**Fig. 3 | Moiré growth mechanisms. a, b**, Simulated lattice parameter dependence of the edge strain energy, bulk strain energy and interlayer interaction energy for triangular MoS<sub>2</sub> nuclei on compressively strained MoS<sub>2</sub>.  $L = 13$  nm (**a**),  $L = 153$  nm (**b**) (details in Methods). The arrows indicate the lattice-matched and relaxed lattice parameters. **c, d**, Energy versus lattice parameter of the top layer for triangular nuclei of increasing  $L$ . The lattice constant of the bottom layer is shortened by 0.034 Å in **c** and 0.052 Å in **d**. The vertical dashed lines indicate the lattice parameter of the WS<sub>2</sub> bottom layer. The arrow illustrates the path followed by growing nuclei to minimize their energy. The dashed arrow shows the transition from the metastable lattice-matched state to the relaxed state and the insets depict the corresponding growth modes. Individual curves are vertically displaced for clarity. **e**, Schematic of the moiré growth modes (depicted in the insets) as a function of the edge stress ( $\tau_{edge}$ ), bulk strain ( $\epsilon$ ), bulk strain energy and interlayer interaction energy. **f, g**, Schematic

of the moiré formation process from metastable strained nuclei. This growth mode corresponds to the yellow region in **e, g**. Schematic of the direct moiré formation mechanism. This growth mode corresponds to the green region in **e, h, i**. Large-scale TEM micrograph of relaxed continuous WS<sub>0.35</sub>Se<sub>1.65</sub>/WS<sub>1.88</sub>Se<sub>0.12</sub> showing a homogeneous moiré pattern, likely formed by the direct moiré growth mode. **i**, TEM micrograph of a 150 nm WS<sub>1.12</sub>Se<sub>0.88</sub> nucleus on WS<sub>1.88</sub>Se<sub>0.12</sub>. **j**, TEM micrograph of a WS<sub>1.42</sub>Se<sub>0.58</sub> nucleus on WS<sub>1.75</sub>Se<sub>0.25</sub> after uniaxial strain relaxation nucleation at its corners. The white arrow indicates uniaxial stress relaxation nucleating at corners, evidenced by parallel one-dimensional (1D) moiré stripes with a periodicity of ~35 nm. The red circle shows the beginning of biaxial strain relaxation at the edges. The brightness and contrast are locally adjusted to reduce the visibility of electron-beam-induced contamination spots (uncorrected image is shown in Supplementary Fig. 11).

is sufficient, aligned moirés become the thermodynamically stable configuration (middle region of Fig. 3e). For a given  $\Delta E_{int}$ , the magnitude and sign of the edge and bulk stress can be expected to lead to the two aligned moiré growth modes illustrated in Fig. 3f, g. If  $\Delta a$  is relatively small, such as in Fig. 3c ( $\Delta a = 0.034$  Å), nuclei can get trapped in the lattice-matched configuration, which eventually becomes a metastable state as the nuclei grow. Nuclei can then transition to the stable relaxed

configuration (dashed arrow in Fig. 3c) and form a stable moiré, which expands by lateral growth, as illustrated in Fig. 3f. The metastable state formation is driven by the minimum of  $E_{int}$  in the lattice-matched configuration and by edge stress, which resists relaxation when its sign is opposite to the bulk stress. However, since  $U_{edges}$  scales as  $1/L$ , the relaxed state becomes increasingly favoured as the nuclei grow. Moreover, the metastable state can form even without edge stress,

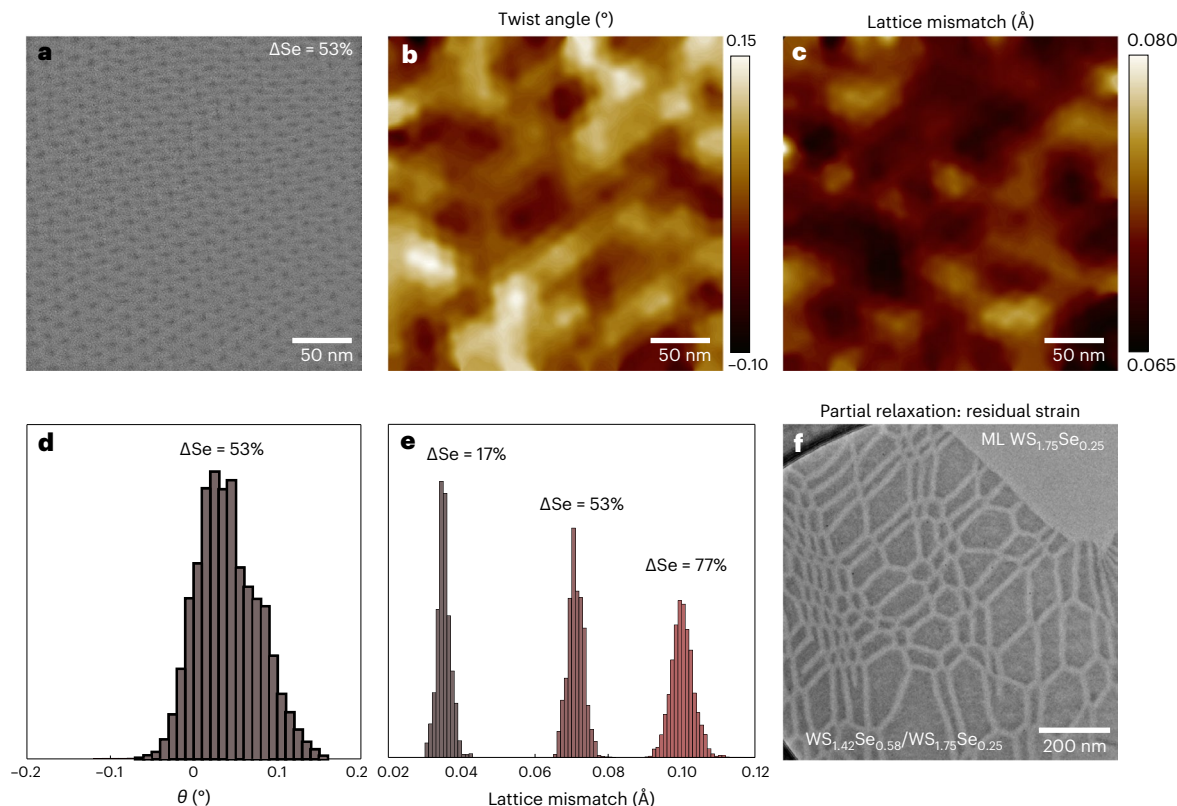


**Fig. 4 | Moiré uniformity.** **a**, TEM micrograph of the moiré of  $\text{WS}_{0.82}\text{Se}_{1.18}/\text{WS}_{1.88}\text{Se}_{0.12}$  ( $\Delta\text{Se} = 53\%$ ). **b**, Map of the local twist angle for the image in **a**, calculated using the fitted moiré lattice vectors at each lattice site. **c**, Map of the local lattice mismatch for the image in **a**. **d**, Histogram of the local twist angle for

the image in **a** and **b**. **e**, Histograms of the local lattice mismatch for samples with various compositions. **f**, TEM micrograph of a partially relaxed  $\text{WS}_{1.42}\text{Se}_{0.58}/\text{WS}_{1.75}\text{Se}_{0.25}$  flake showing large residual strain. ML, monolayer.

due to the narrowing of  $E_{\text{int}}$ , as detailed in Supplementary Fig. 10. The conditions favouring this growth mode are summarized by the yellow region in Fig. 3e. The second growth mode (green region in Fig. 3e) is believed to arise when the lattice-matched metastable state is never favoured, such as for  $\Delta a = 0.052 \text{ \AA}$  as in Fig. 3d. This occurs at larger  $\Delta a$ , or when the edge stress is small or has the same sign as the bulk stress (which can be achieved by reversing the growth order in this work, for instance). These conditions can be expected to lead to direct moiré growth, where relaxed moirés grow laterally immediately after nucleation, as shown in Fig. 3g. A large-scale moiré likely formed by direct moiré growth, given the large  $\Delta a$  ( $\Delta\text{Se} = 77\%$ ), is presented in Fig. 3h. Furthermore, as  $\Delta a$  increases further, random rotational misalignment of the two layers is eventually expected, as happens in many materials systems<sup>42</sup> (right side of Fig. 3e).

TEM images of the early stages of the aligned moiré growth for  $\Delta\text{Se} = 38\%$  and  $17\%$  are displayed in Fig. 3i,j, respectively. At  $\Delta\text{Se} = 38\%$ , small nuclei (150 nm) already display a moiré pattern (Fig. 3i), which suggests that they formed through direct moiré growth, in agreement with previous experiments on vdW systems with substantial  $\Delta a$  (refs. 43,44). A different behaviour, associated with the other moiré growth mode, is observed for  $\Delta\text{Se} = 17\%$ . Figure 3j shows a large ( $\sim 1 \mu\text{m}$ ) nucleus ( $\Delta\text{Se} = 17\%$ ) with ongoing stress relaxation, which implies the presence of a metastable lattice-matched state in vdW HSs with small  $\Delta a$ . No moiré is observed on most of the nucleus area, indicating that despite the chalcogen ratio difference between the two layers, the epitaxial configuration is favoured during nucleation. Interestingly, this intermediate state provides insight into the stress relaxation mechanisms. Given the nucleus size and corrugation of the interlayer interaction energy<sup>45</sup>, the energy barrier for concerted relaxation can reach tens of kiloelectronvolts. This means that relaxed regions must

nucleate first and then grow. Relaxation cannot nucleate in the bulk since it would be surrounded by an energetically prohibitive, highly stressed region or create wrinkles. Hence, stress relaxation is expected to nucleate by slipping at the edges or corner of the nuclei. The TEM image in Fig. 3j confirms that stress relaxation nucleates at the nuclei's corners, as indicated by the parallel stripes (one-dimensional moiré). The orientation of the stripes implies that corners are first pushed out to relieve stress uniaxially, parallel to the corner's bisector. Indeed, the periodicity of the outermost stripes is  $\sim 35 \text{ nm}$ , meaning that the stress is fully relieved in one direction at the corners. However, the nucleus is still strained in the other direction, suggesting that the edges of the triangle are pinned to the bottom layer. Nonetheless, biaxial stress relaxation (stripes at  $\sim 60^\circ$  from the parallel stripes) is seen at the edges of the nucleus (red circle in Fig. 3j) and may occur at a later stage.

## Moiré uniformity

The moiré uniformity is closely related to the growth and stress relaxation mechanisms. We analysed the strain and twist angle uniformity by fitting the moiré lattice vectors in TEM images such as the one in Fig. 4a for  $\Delta\text{Se} = 53\%$ . Using the average reciprocal lattice vectors of the bottom layer, measured in the FFT, we then calculated the top layer lattice vectors for every moiré unit cell with  $\mathbf{k}_{\text{moiré}} = \mathbf{k}_{\text{WS}_x\text{Se}_{2-x}} - \mathbf{k}_{\text{WS}_y\text{Se}_{2-y}}$ . The average twist angles ( $\theta$ ) of the analysed samples ( $\Delta\text{Se}$  of 17–77%) are  $<0.037^\circ$ , and local fluctuations of  $0.02$ – $0.06^\circ$  (standard deviation, s.d.) are observed in the analysed regions ( $\sim 250 \times 250 \text{ nm}^2$ ), as illustrated in Fig. 4b for  $\Delta\text{Se} = 53\%$ . Figure 4c shows the local variations of the lattice mismatch, which are on the order of  $0.0018$ – $0.0028 \text{ \AA}$  (s.d.). The twist angle distribution for  $\Delta\text{Se} = 53\%$  is shown in Fig. 4d, and Fig. 4e presents the lattice mismatch distributions for three different compositions. The small

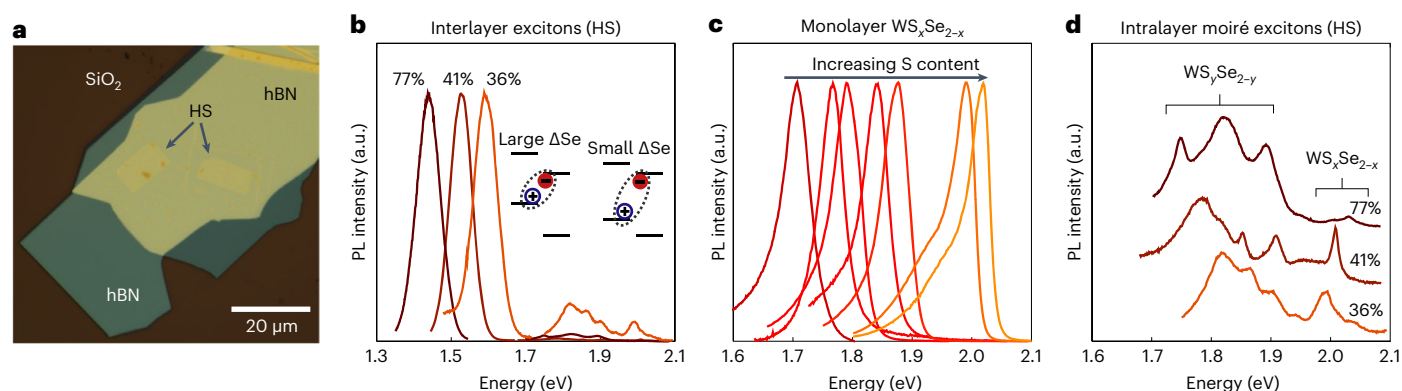


**Fig. 5 | Excitons in grown moiré vdW HSs.** **a**, Optical micrograph of  $\text{WS}_{0.35}\text{Se}_{1.65}/\text{WS}_{1.88}\text{Se}_{0.12}$  encapsulated with exfoliated hBN flakes. **b**, PL spectra ( $T = 77\text{ K}$ ) of three  $\text{WS}_y\text{Se}_{2-y}/\text{WS}_x\text{Se}_{2-x}$  vdW HSs ( $\Delta\text{Se} = 77\%$  (brown),  $\Delta\text{Se} = 41\%$  (dark red) and  $\Delta\text{Se} = 36\%$  (orange)). The spectra are dominated by the interlayer exciton (between 1.6 and 1.3 eV). **c**, PL spectra of monolayer  $\text{WS}_x\text{Se}_{2-x}$  flakes with various

compositions grown on  $\text{SiO}_2/\text{Si}$ . **d**, Close-up of the PL spectra in **b** showing the intralayer moiré excitons of the  $\text{WS}_y\text{Se}_{2-y}$  Se-rich top layer (1.75–1.91 eV). No clear splitting of the intralayer exciton peak of the  $\text{WS}_x\text{Se}_{2-x}$  S-rich bottom layer is observed (1.99–2.04 eV).

nonuniformities of the strain and twist angle (Fig. 4b–e) may originate from statistical fluctuations of the chalcogen distributions and/or residual stresses in the layers. However, statistical analyses of STEM measurements suggest that chalcogen segregation is unlikely (Supplementary Figs. 12–14). Instead, small stresses may form during lateral growth of the top layer, due to the competition between the local minimization of  $E_{\text{int}}$  and  $U_{\text{bulk}}$ . On the other hand, due to the absence of long-range order on the  $\text{SiO}_2$  surface, such stresses are not expected to form during the bottom layer's growth. Moreover, previous studies indicate that the stress induced by the thermal expansion coefficient mismatch with  $\text{SiO}_2/\text{Si}$  is not released after the cool-down of the bottom layer (except near flake edges)<sup>46–48</sup>. Since the two layers are grown at the same temperature, the bottom layer is therefore expected to be mostly strain-free and uniform during the second growth step, thus not introducing additional substantial nonuniformity.

While vdW HSs with substantial  $\Delta a$  values typically display uniform moirés (Supplementary Fig. 15), irregular moirés with a long periodicity can form in vdW HSs with very small  $\Delta a$  values, especially in smaller flakes. In fact, when the  $E_{\text{int}}$  and  $U_{\text{bulk}}$  are comparable (for example,  $\Delta\text{Se} = 17\%$ ), nuclei can be trapped in the metastable lattice-matched configuration. The reduced driving force for relaxation can thus lead to the presence of residual strain such as in Fig. 4f. In fact, relaxation is not rapid enough to be completed before a substantial area is grown. Both relaxed regions (for example, in Fig. 2d) and partially strained regions (Fig. 4f) are observed at  $\Delta\text{Se} = 17\%$ , which suggests that this composition approaches the lower limit for moiré formation.

Inverting the two growth steps could promote stress relaxation and improve uniformity in samples with very small  $\Delta a$  values. Since edge stress is expected to be tensile in TMDCs<sup>40</sup>, it competes with the compressive bulk stress of the top Se-rich layer. This favours the metastable lattice-matched state and increases the energy barrier for relaxation. However, if S-rich  $\text{WS}_y\text{Se}_{2-y}$  is grown on Se-rich  $\text{WS}_x\text{Se}_{2-x}$ , the bulk stress of the nuclei would be tensile. The tensile edge stress would therefore be an additional driving force for relaxation, which could lead to early stress relaxation or even promote the direct moiré growth mode. Moreover, this may allow one to realize even larger moiré periodicities by promoting stress relaxation in vdW HSs with smaller  $\Delta a$  values. Other strategies might improve the uniformity of moirés with small  $\Delta a$  values, including using a higher temperature and lower growth rate, or implementing a two-step growth process with favourable stress relaxation followed by lateral growth of the desired composition. The growth of such lateral heterostructures needs to be carefully controlled, as they can also induce strain and moiré nonuniformity (Supplementary Fig. 16).

## Excitons in grown moiré heterostructures

Next, we look at the photoluminescence (PL) of  $\text{WS}_y\text{Se}_{2-y}/\text{WS}_x\text{Se}_{2-x}$ . To improve the emission intensity, the HSs were removed from the growth substrate and encapsulated with hBN for optical measurements (Fig. 5a)<sup>49</sup>. The PL (532 nm excitation; temperature,  $T = 77\text{ K}$ ) is dominated by interlayer exciton recombination due to the rapid charge transfer at the vdW interface<sup>50</sup> (Fig. 5b).  $\text{WS}_y\text{Se}_{2-y}/\text{WS}_x\text{Se}_{2-x}$  is expected to form type II HSs for all compositions<sup>51,52</sup>, and therefore electrons (holes) generated in the selenium-rich (sulfur-rich) layer transfer to the sulfur-rich (selenium-rich) layer to form the interlayer exciton (Fig. 5b). Expectedly, the interlayer exciton peak position (1.44 eV) for  $\Delta\text{Se} = 77\%$  is blueshifted from previous results on  $\text{WSe}_2/\text{WS}_2$  (1.41 eV)<sup>6</sup>. Furthermore, as  $\Delta\text{Se}$  decreases to 36%, the interlayer exciton PL peak blueshifts from 1.44 eV to 1.59 eV due to the shrinking band offset.

As-grown monolayer  $\text{WS}_x\text{Se}_{2-x}$  displays a single peak associated with the A exciton that blueshifts with increasing S content (Fig. 5c)<sup>53</sup>. In the vdW HSs, PL from the intralayer A excitons of both layers can be observed, as shown in Fig. 5d. The intralayer exciton emission intensity is typically ~10–100 times weaker than the interlayer exciton one (Fig. 5b). Furthermore, the signal of the Se-rich layer is larger than the signal of the S-rich layer. As in minimally twisted  $\text{WSe}_2/\text{WS}_2$  and  $\text{MoSe}_2/\text{MoS}_2$ , the A exciton of the Se-rich layer splits into three peaks in the vdW HSs, due to the formation of exciton minibands in the moiré potential<sup>6,10</sup>. For  $\Delta\text{Se} = 77\%$ , the peaks are located at 1.74, 1.82 and 1.89 eV (brown curve in Fig. 5d), slightly blueshifted from previous measurements on mechanically exfoliated and stacked  $\text{WSe}_2/\text{WS}_2$  (ref. 6). Nonetheless, the 150 meV splitting is larger than in minimally twisted  $\text{WSe}_2/\text{WS}_2$  (~100 meV), which may be due to the stronger interlayer coupling in grown samples. Expectedly, as the top layer S content increases, the moiré intralayer exciton peaks blueshift. We also note some spatial variation of the peak positions and intensities for the intralayer moiré excitons (Supplementary Fig. 17), which may be associated with nonuniformities introduced during the transfer process. Nonetheless, these results demonstrate that intralayer moiré excitons form in grown vdW HSs, thus providing a pathway to harness them in future quantum technologies<sup>5–9</sup>.

## Summary and outlook

In summary, we demonstrated that substitutional alloying of S/Se allows for the thermodynamically driven growth of TMDC vdW HSs with tunable moiré periods. Furthermore, we identified the critical role of bulk and edge stress in shaping the conditions favourable to moiré formation and the resulting moiré growth modes. At a large lattice mismatch, rotationally aligned, relaxed moirés grow directly



after nucleation. Our results suggest that at a small lattice mismatch, metastable lattice-matched nuclei can form first and may reach lateral dimensions of up to a micrometre. Stress relaxation then nucleates at the corners of the nuclei and spreads into the bulk, which can allow for lateral growth of relaxed moirés. This understanding can be harnessed to control large-scale synthesis and engineer novel moiré nanostructures, representing a critical step for the integration of moiré vdWHSs in emerging quantum technologies.

Considering the recent progress on the wafer-scale growth of single-crystal monolayer TMDCs<sup>37,38</sup>, combining our approach with nucleation engineering and kinetics control to obtain pure 2H or 3R stacking (Supplementary Fig. 5) will allow for the extension of moiré epitaxy to the wafer scale<sup>26,35,36,39</sup>. Furthermore, alloying can be extended to tune other moiré materials containing *p*-block elements, such as other TMDCs, 2D pnictogen alloys<sup>54</sup>, magnetic metal halides<sup>55</sup> and so on. With the recent progress on the synthesis of 2D silicon–carbon alloys<sup>56</sup>, graphene/2D-C<sub>x</sub>Si<sub>1-x</sub> vdWHSs with only ~3.5% silicon<sup>57</sup> could be targeted to reproduce some of the properties of magic-angle twisted bilayer graphene at the wafer scale. Alloying in vdWHSs therefore provides a broad range of opportunities for the large-scale growth of tunable moiré materials.

## Online content

Any methods, additional references, Nature Portfolio reporting summaries, source data, extended data, supplementary information, acknowledgements, peer review information; details of author contributions and competing interests; and statements of data and code availability are available at <https://doi.org/10.1038/s41563-023-01596-z>.

## References

- Rong, Z. Y. & Kuiper, P. Electronic effects in scanning tunneling microscopy: moiré pattern on a graphite surface. *Phys. Rev. B* **48**, 17427–17431 (1993).
- Bistritzer, R. & MacDonald, A. H. Moiré bands in twisted double-layer graphene. *Proc. Natl Acad. Sci. USA* **108**, 12233–12237 (2011).
- Kim, K. et al. Van der Waals heterostructures with high accuracy rotational alignment. *Nano Lett.* **16**, 1989–1995 (2016).
- Kim, K. et al. Tunable moiré bands and strong correlations in small-twist-angle bilayer graphene. *Proc. Natl Acad. Sci. USA* **114**, 3364–3369 (2017).
- Alexeev, E. M. et al. Resonantly hybridized excitons in moiré superlattices in van der Waals heterostructures. *Nature* **567**, 81–86 (2019).
- Jin, C. et al. Observation of moiré excitons in WSe<sub>2</sub>/WS<sub>2</sub> heterostructure superlattices. *Nature* **567**, 76 (2019).
- Seyler, K. L. et al. Signatures of moiré-trapped valley excitons in MoSe<sub>2</sub>/WSe<sub>2</sub> heterobilayers. *Nature* **567**, 66 (2019).
- Tran, K. et al. Evidence for moiré excitons in van der Waals heterostructures. *Nature* **567**, 71 (2019).
- Yu, H., Liu, G.-B., Tang, J., Xu, X. & Yao, W. Moiré excitons: from programmable quantum emitter arrays to spin-orbit-coupled artificial lattices. *Sci. Adv.* **3**, e1701696 (2017).
- Zhang, N. et al. Moiré intralayer excitons in a MoSe<sub>2</sub>/MoS<sub>2</sub> heterostructure. *Nano Lett.* **18**, 7651–7657 (2018).
- Cao, Y. et al. Correlated insulator behaviour at half-filling in magic-angle graphene superlattices. *Nature* **556**, 80–84 (2018).
- Cao, Y. et al. Unconventional superconductivity in magic-angle graphene superlattices. *Nature* **556**, 43–50 (2018).
- Yankowitz, M. et al. Tuning superconductivity in twisted bilayer graphene. *Science* **363**, 1059–1064 (2019).
- Sharpe, A. L. et al. Emergent ferromagnetism near three-quarters filling in twisted bilayer graphene. *Science* **365**, 605–608 (2019).
- Kennes, D. M. et al. Moiré heterostructures as a condensed-matter quantum simulator. *Nat. Phys.* **17**, 155–163 (2021).
- Ma, C. et al. Intelligent infrared sensing enabled by tunable moiré quantum geometry. *Nature* **604**, 266–272 (2022).
- Mak, K. F. & Shan, J. Semiconductor moiré materials. *Nat. Nanotechnol.* **17**, 686–695 (2022).
- Lee, J.-H. et al. Wafer-scale growth of single-crystal monolayer graphene on reusable hydrogen-terminated germanium. *Science* **344**, 286–289 (2014).
- Ahn, S. J. et al. Dirac electrons in a dodecagonal graphene quasicrystal. *Science* **361**, 782–786 (2018).
- Sun, L. et al. Hetero-site nucleation for growing twisted bilayer graphene with a wide range of twist angles. *Nat. Commun.* **12**, 2391 (2021).
- Liu, C. et al. Designed growth of large bilayer graphene with arbitrary twist angles. *Nat. Mater.* **21**, 1263–1268 (2022).
- Yang, W. et al. Epitaxial growth of single-domain graphene on hexagonal boron nitride. *Nat. Mater.* **12**, 792–797 (2013).
- Lin, Y.-C. et al. Atomically thin resonant tunnel diodes built from synthetic van der Waals heterostructures. *Nat. Commun.* **6**, 7311 (2015).
- Li, B. et al. Direct vapor phase growth and optoelectronic application of large band offset SnS<sub>2</sub>/MoS<sub>2</sub> vertical bilayer heterostructures with high lattice mismatch. *Adv. Electron. Mater.* **2**, 1600298 (2016).
- Li, X. et al. Two-dimensional GaSe/MoSe<sub>2</sub> misfit bilayer heterojunctions by van der Waals epitaxy. *Sci. Adv.* **2**, e1501882 (2016).
- Fu, D. et al. Molecular beam epitaxy of highly crystalline monolayer molybdenum disulfide on hexagonal boron nitride. *J. Am. Chem. Soc.* **139**, 9392–9400 (2017).
- Yang, T. et al. Van der Waals epitaxial growth and optoelectronics of large-scale WSe<sub>2</sub>/SnS<sub>2</sub> vertical bilayer p–n junctions. *Nat. Commun.* **8**, 1906 (2017).
- Carozo, V. et al. Excitonic processes in atomically-thin MoSe<sub>2</sub>/MoS<sub>2</sub> vertical heterostructures. *2D Mater.* **5**, 031016 (2018).
- Fu, Q. et al. One-step synthesis of metal/semiconductor heterostructure NbS<sub>2</sub>/MoS<sub>2</sub>. *Chem. Mater.* **30**, 4001–4007 (2018).
- Wu, R. et al. Van der Waals epitaxial growth of atomically thin 2D metals on dangling-bond-free WSe<sub>2</sub> and WS<sub>2</sub>. *Adv. Funct. Mater.* **29**, 1806611 (2019).
- Wu, X. et al. Vapor growth of WSe<sub>2</sub>/WS<sub>2</sub> heterostructures with stacking dependent optical properties. *Nano Res.* **12**, 3123–3128 (2019).
- Zheng, W. et al. Direct vapor growth of 2D vertical heterostructures with tunable band alignments and interfacial charge transfer behaviors. *Adv. Sci.* **6**, 1802204 (2019).
- Li, J. et al. General synthesis of two-dimensional van der Waals heterostructure arrays. *Nature* **579**, 368–374 (2020).
- Li, B. et al. Van der Waals epitaxial growth of air-stable CrSe<sub>2</sub> nanosheets with thickness-tunable magnetic order. *Nat. Mater.* **20**, 818–825 (2021).
- Chen, L. et al. Step-edge-guided nucleation and growth of aligned WSe<sub>2</sub> on sapphire via a layer-over-layer growth mode. *ACS Nano* **9**, 8368–8375 (2015).
- Zhang, X. et al. Defect-controlled nucleation and orientation of WSe<sub>2</sub> on hBN: a route to single-crystal epitaxial monolayers. *ACS Nano* **13**, 3341–3352 (2019).
- Chubarov, M. et al. Wafer-scale epitaxial growth of unidirectional WS<sub>2</sub> monolayers on sapphire. *ACS Nano* **15**, 2532–2541 (2021).
- Wang, J. et al. Dual-coupling-guided epitaxial growth of wafer-scale single-crystal WS<sub>2</sub> monolayer on vicinal a-plane sapphire. *Nat. Nanotechnol.* **17**, 33–38 (2022).
- Liu, L. et al. Uniform nucleation and epitaxy of bilayer molybdenum disulfide on sapphire. *Nature* **605**, 69–75 (2022).
- Deng, J., Fampiou, I., Liu, J. Z., Ramasubramaniam, A. & Medhekar, N. V. Edge stresses of non-stoichiometric edges in two-dimensional crystals. *Appl. Phys. Lett.* **100**, 251906 (2012).

41. Liu, J. et al. Interpretable molecular models for molybdenum disulfide and insight into selective peptide recognition. *Chem. Sci.* **11**, 8708–8722 (2020).
42. Fortin-Deschênes, M. et al. Dynamics of antimonene–graphene van der Waals growth. *Adv. Mater.* **31**, 1900569 (2019).
43. Coraux, J. et al. Growth of graphene on Ir(111). *New J. Phys.* **11**, 023006 (2009).
44. Tetlow, H. et al. Growth of epitaxial graphene: theory and experiment. *Phys. Rep.* **542**, 195–295 (2014).
45. Levita, G., Molinari, E., Polcar, T. & Righi, M. C. First-principles comparative study on the interlayer adhesion and shear strength of transition-metal dichalcogenides and graphene. *Phys. Rev. B* **92**, 085434 (2015).
46. Amani, M. et al. Growth-substrate induced performance degradation in chemically synthesized monolayer MoS<sub>2</sub> field effect transistors. *Appl. Phys. Lett.* **104**, 203506 (2014).
47. Liu, Z. et al. Strain and structure heterogeneity in MoS<sub>2</sub> atomic layers grown by chemical vapour deposition. *Nat. Commun.* **5**, 5246 (2014).
48. Chae, W. H., Cain, J. D., Hanson, E. D., Murthy, A. A. & Dravid, V. P. Substrate-induced strain and charge doping in CVD-grown monolayer MoS<sub>2</sub>. *Appl. Phys. Lett.* **111**, 143106 (2017).
49. Ajayi, O. A. et al. Approaching the intrinsic photoluminescence linewidth in transition metal dichalcogenide monolayers. *2D Mater.* **4**, 031011 (2017).
50. Hong, X. et al. Ultrafast charge transfer in atomically thin MoS<sub>2</sub>/WS<sub>2</sub> heterostructures. *Nat. Nanotechnol.* **9**, 682–686 (2014).
51. Kang, J., Tongay, S., Zhou, J., Li, J. & Wu, J. Band offsets and heterostructures of two-dimensional semiconductors. *Appl. Phys. Lett.* **102**, 012111 (2013).
52. Zhou, S., Ning, J., Sun, J. & Srolovitz, D. J. Composition-induced type I and direct bandgap transition metal dichalcogenides alloy vertical heterojunctions. *Nanoscale* **12**, 201–209 (2020).
53. Duan, X. et al. Synthesis of WS<sub>2</sub>Se<sub>2–2x</sub> alloy nanosheets with composition-tunable electronic properties. *Nano Lett.* **16**, 264–269 (2016).
54. Fortin-Deschênes, M. et al. 2D antimony–arsenic alloys. *Small* **16**, 1906540 (2020).
55. Kezilebieke, S. et al. Electronic and magnetic characterization of epitaxial CrBr<sub>3</sub> monolayers on a superconducting substrate. *Adv. Mater.* **33**, 2006850 (2021).
56. Gao, Z.-Y. et al. Experimental realization of atomic monolayer Si<sub>9</sub>C<sub>15</sub>. *Adv. Mater.* **34**, 2204779 (2022).
57. Vogt, P. et al. Silicene: compelling experimental evidence for graphenelike two-dimensional silicon. *Phys. Rev. Lett.* **108**, 155501 (2012).
58. Weston, A. et al. Atomic reconstruction in twisted bilayers of transition metal dichalcogenides. *Nat. Nanotechnol.* **15**, 592–597 (2020).

**Publisher's note** Springer Nature remains neutral with regard to jurisdictional claims in published maps and institutional affiliations.

Springer Nature or its licensor (e.g. a society or other partner) holds exclusive rights to this article under a publishing agreement with the author(s) or other rightsholder(s); author self-archiving of the accepted manuscript version of this article is solely governed by the terms of such publishing agreement and applicable law.

© The Author(s), under exclusive licence to Springer Nature Limited 2023



## Methods

### Two-step growth of $\text{WS}_y\text{Se}_{2-y}/\text{WS}_x\text{Se}_{2-x}$

The two-step CVD growth of  $\text{WS}_y\text{Se}_{2-y}/\text{WS}_x\text{Se}_{2-x}$  is done on 300 nm  $\text{SiO}_2/\text{Si}$  substrates ( $2 \times 2 \text{ cm}^2$ ) cleaned by ultrasonication in acetone, isopropanol and deionized water for 5 minutes each. For the growth of the first monolayer (sulfur-rich  $\text{WS}_x\text{Se}_{2-x}$ ), the substrate is placed face-down on a quartz boat containing 15 mg  $\text{WO}_{2.9}$  powder (Alfa Aesar, 99.99%) and 0.5–1 mg NaCl (ref. 59). The substrate is positioned at the centre of a one-zone furnace in a 2 inch quartz tube. Then 70 mg sulfur powder (Sigma Aldrich, 99.98%) is placed upstream, 1 cm out of the furnace ( $\sim 200^\circ\text{C}$ ), and selenium (Beantown Chemical, 99.999%) is provided by the background pressure originating from the growth of  $\text{WS}_x\text{Se}_{2-x}$  with higher Se content, carried out in the same tube. This leads to a Se content of  $\sim 6$ –12% in the first layer. Before growth, two cycles of pumping (down to 10 mtorr) and purging with Ar (99.999%) are done to remove  $\text{H}_2\text{O}$  and  $\text{O}_2$ . The growth is carried out at atmospheric pressure under 200 sccm Ar flow. The temperature is ramped at a rate of  $25^\circ\text{C min}^{-1}$  and held at  $850^\circ\text{C}$  for 6 min. The furnace is then cooled to room temperature using an air pump, and the samples are taken out and stored in a glove box.

In the second step, monolayer  $\text{WS}_y\text{Se}_{2-y}$  with a higher Se content is grown on  $\text{WS}_x\text{Se}_{2-x}/\text{SiO}_2/\text{Si}$  using the same method. Some 100–130 mg  $\text{WO}_{2.9}$  and 18–27 mg NaCl are used with 200 sccm of 10%  $\text{H}_2$  in Ar as the carrier gas (99.999%). To control the sulfur-to-selenium ratio in the grown  $\text{WS}_y\text{Se}_{2-y}$ , we independently change the quantity and temperature of the Se and S precursors. Some 0–25 mg sulfur powder and 20–30 mg selenium powder are used, and their respective temperature is controlled by their position in the furnace (1.25–3 cm outside the furnace for S and 0–0.75 cm inside the furnace for Se). The estimated Se temperature is  $\sim 400^\circ\text{C}$ . We note that a substantial amount of precursor S and Se evaporates from the tube's wall, and thus the composition of the grown layers depends on the growth history. Nonetheless, in a sequence of four growths with increasing Se/S mass ratios of 0.8, 1.33, 2 and 2.5, we obtained Se contents in the top layer of 29%, 42%, 47% and 59%, respectively. To obtain reproducible growth conditions or pure  $\text{WS}_2$  or  $\text{WS}_x$ , a dedicated tube should be used for each composition.

### Transmission electron microscopy

For TEM characterization,  $\text{WS}_y\text{Se}_{2-y}/\text{WS}_x\text{Se}_{2-x}$  vdW HSs are transferred onto lacey carbon on Cu mesh grids (Ted Pella) using an etching-free transfer method with a polymethyl methacrylate (PMMA) film<sup>60</sup>. To minimize damage to the HS, ultrasonication at low power (25 W,  $\sim 10$ –30 s) is used to detach the PMMA/ $\text{WS}_y\text{Se}_{2-y}/\text{WS}_x\text{Se}_{2-x}$  from the substrate only when needed. Detaching the grown layers from the substrate is expected to release the stress introduced by the difference in thermal expansion coefficients between TMDCs and the substrate. TMDCs grown at  $850^\circ\text{C}$  on  $\text{SiO}_2/\text{Si}$  do not release stress upon cool-down<sup>46–48</sup>, and the two growth steps are carried out at the same temperature. This means that detaching the layers is expected to restore stress-free conditions, almost identical to the growth conditions of the second step. Importantly, after being released from the substrate, the bottom layer is no longer restrained by the substrate. The stress in lattice-matched regions of the top layer can therefore be redistributed in both layers to form a more stable configuration. Releasing the layers is therefore not expected to promote stress relaxation in the top layer.

TEM is carried out using an FEI Tecnai Osiris microscope operated at 200 kV in TEM bright-field mode. High-pass FFT filtering is done to reduce the visibility of long-range contrast variations. Smoothing is done for noise reduction. Energy-dispersive X-ray spectroscopy is done in TEM mode. The selenium content is determined using the ratio of the selenium L $\alpha$  peak to the tungsten M $\alpha$  peak of  $\text{WS}_y\text{Se}_{2-y}/\text{WS}_x\text{Se}_{2-x}$ .  $\text{WS}_2$  powder is used as a reference to calibrate the compositions. The Se content from the bottom monolayer  $\text{WS}_x\text{Se}_{2-x}$  regions is subtracted from the total content to determine the top  $\text{WS}_y\text{Se}_{2-y}$  composition and compute  $\Delta\text{Se}$ . If no  $\text{WS}_x\text{Se}_{2-x}$  regions are present (such as in a continuous HS),

the Se content of the bottom layer is measured on  $\text{WS}_x\text{Se}_{2-x}$  grown in identical conditions. Due to the small size of the 150 nm nucleus presented in Fig. 3i, electron beam damage prevents the direct measurement of its composition. We therefore determine the composition using slightly larger nuclei (300 nm). Given their similar small size, both nuclei likely formed approximately at the same time, and therefore under the same conditions.

### Atomic-resolution STEM

Atomic-resolution STEM is carried out using a Thermo Fisher Scientific Themis Z G3 60–300 kV S/TEM instrument operated at 60 kV with a 10–65 pA beam current and 20–40 mrad convergence angle. Atomic-resolution images are collected using a high-angle annular dark-field detector with a collection angle of 64–200 mrad. High-pass FFT filtering is done in all atomic-resolution STEM images to reduce the visibility of carbon contamination, and smoothing is done for noise reduction.

### STEM image simulations

STEM image simulations are done using the Prismatic software<sup>61</sup>. The simulation parameters (acceleration voltage, convergence angle, detector collection angle) are set according to experimental parameters. The aberration coefficients are set to zero.

### Photoluminescence

Micro-PL measurements are done using a  $\times 40$  (numerical aperture, 0.6) objective with 532 nm excitation at 77 K. Due to the PL quenching observed in as-grown  $\text{WS}_y\text{Se}_{2-y}/\text{WS}_x\text{Se}_{2-x}$  on  $\text{SiO}_2/\text{Si}$ , the vdW HSs are encapsulated with hBN. First, the HSs are transferred to clean  $\text{SiO}_2/\text{Si}$  substrates with the same method used for transfer to TEM grids. To facilitate encapsulation, the lateral size of the HS is reduced to  $\sim 10 \mu\text{m}$  by reactive ion etching ( $\text{CHF}_3/\text{O}_2$ ). After hBN encapsulation, contaminants are squeezed out of the interface using an atomic force microscope tip in contact mode<sup>62</sup>.

### Modelling of the energy of nuclei

We model the energy of the triangular TMDCs nuclei on lattice-mismatched monolayer TMDC. Since the mechanical properties and interlayer interactions of Mo- and W-based TMDCs are almost identical, and since accurate interatomic potentials for  $\text{WS}_x\text{Se}_{2-x}$  are not available, we base our modelling on the force field developed by Liu et al. for  $\text{MoS}_2$  (ref. 41). This model has been found to reproduce the mechanical properties and interlayer interactions of  $\text{MoS}_2$  very accurately. The interatomic interactions are given by the following<sup>41</sup>:

$$E_{\text{pot}} = \sum_{ij \text{ bonded}} K_{r,ij} (r_{ij} - r_{0,ij})^2 + \sum_{ijk \text{ bonded}} K_{\theta,ijk} (\theta_{ijk} - \theta_{0,ijk})^2 \\ + \frac{1}{4\pi\epsilon_0} \sum_{\text{nonbonded}} \frac{q_i q_j}{r_{ij}} + \sum_{\text{nonbonded}} \epsilon_{ij} \left[ 2 \left( \frac{\sigma_{ij}}{r_{ij}} \right)^9 - 3 \left( \frac{\sigma_{ij}}{r_{ij}} \right)^6 \right].$$

(1, 3 excluded)                      (1, 3 excluded)

The two first terms on the right-hand side are used for the covalently bonded atoms. The  $r_{ij}$  and  $\theta_{ijk}$  are the interatomic distances and bond angles;  $r_{0,ij}$  and  $\theta_{0,ijk}$  are the equilibrium lengths and bond angles; and  $K_{r,ij}$  and  $K_{\theta,ijk}$  are the harmonic bond stretching constants and angle bending constants. The two last terms on the right-hand side are the long-range interactions between non-bonded atoms;  $q_i$  are the atomic charges, and  $\epsilon_{ij}$  and  $\sigma_{ij}$  are the Lennard-Jones potential parameters. Additional details about the parameters can be found in ref. 41. The intralayer interactions are heavily dominated by the bonded terms. Therefore, given the large size of our system, we apply only the non-bonded terms to interlayer interactions for computational efficiency, as explained in the following.

To model the lattice mismatch, we modify the lattice parameter of the bottom layer and fix its atomic structure. The lattice mismatch

is equivalent to  $\Delta\text{Se}(a_{\text{WSe}_2} - a_{\text{WS}_2})$ , where  $a_{\text{WS}_2} = 3.153 \text{ \AA}$  and  $a_{\text{WSe}_2} = 3.282 \text{ \AA}$  are the equilibrium lattice constants of  $\text{WS}_2$  and  $\text{WSe}_2$ , respectively. Fixing the atomic structure of the bottom layer is believed to modify the computed energies only minimally. In fact, in our growth experiments, the bottom layer is several orders of magnitude larger than the nuclei. This means that the nuclei can easily be strained, since their edges are free to expand and contract. On the other hand, the local expansion of the bottom layer would induce a compression in the surrounding region, which adds an energy prohibitive term. While such a compression could accommodate some of the strain in the nuclei in suspended layers, the  $\text{SiO}_2$  substrate should prevent the formation of strain in the bottom layer in our experiments. In fact, the strain associated with the thermal expansion coefficient mismatch of TMDCs grown on  $\text{SiO}_2$  is not released during cool-down<sup>48</sup>. This implies that they cannot easily slip on  $\text{SiO}_2$  and makes it highly unlikely that stress induced by a nanoscale nucleus would induce slipping of the bottom layer.

Since the bottom layer is frozen, the interlayer interactions can be represented by periodic potentials. We therefore precalculate the non-bonded potentials and their gradients on a  $121 \times 121 \times 481$  grid with the dimensions of the unit cell, extended over 1.3 nm in the out-of-plane direction. This allows us to rapidly compute the forces associated with interlayer interactions. A cut-off radius of 20 unit cells is used for the non-bonded interlayer interactions. This truncation introduces a small electric field due to the partial charges  $q_{\text{Mo}} = 0.5e$  and  $q_{\text{S}} = -0.25e$  ( $e$ , electron charge), which are not fully cancelled in a finite summation. We correct this effect by adding an electric field with opposite sign.

Using this model, we compute the energy of triangular nuclei as a function of their lattice parameter for multiple equilibrium lattice mismatch conditions. For each fixed lattice parameter of the bottom layer, we vary the average lattice parameter of the top layer nuclei by straining their edges (the  $(x, y)$  coordinates of the Mo atoms at the edges are fixed). We then perform the structural optimization of all other coordinates of atoms in the nuclei using a damped molecular dynamics simulation (integrating the equations of motion with an additional damping term):

$$\frac{d^2 \mathbf{r}_i}{dt^2} = \frac{\mathbf{F}_i}{m_i} - \zeta \mathbf{v}_i$$

where  $t$  is time;  $\mathbf{r}_i$ ,  $\mathbf{F}_i$ ,  $m_i$  and  $\mathbf{v}_i$  are the  $(x, y, z)$  coordinates, forces, masses and velocities of atom  $i$ ; and  $\zeta$  is a damping constant. We perform structural optimization until all components of all forces are smaller than  $0.02 \text{ eV \AA}^{-1}$  and then compute the total energy of the nuclei.

## Data availability

Source data are provided with this paper. Other supporting data and very large files are available from the corresponding authors upon reasonable request.

## Code availability

The codes that support the findings of this study are available from the corresponding authors upon reasonable request.

## References

59. Li, S. et al. Halide-assisted atmospheric pressure growth of large  $\text{WSe}_2$  and  $\text{WS}_2$  monolayer crystals. *Appl. Mater. Today* **1**, 60–66 (2015).
60. Ma, D. et al. A universal etching-free transfer of  $\text{MoS}_2$  films for applications in photodetectors. *Nano Res.* **8**, 3662–3672 (2015).
61. Rangel DaCosta, L. et al. Prismatic 2.0 – simulation software for scanning and high resolution transmission electron microscopy (STEM and HRTEM). *Micron* **151**, 103141 (2021).
62. Rosenberger, M. R. et al. Nano-“squeegee” for the creation of clean 2D material interfaces. *ACS Appl. Mater. Interfaces* **10**, 10379–10387 (2018).

## Acknowledgements

STEM images were collected by A. Penn. M.F.-D. acknowledges support from the Natural Sciences and Engineering Research Council of Canada (NSERC) and Fonds de Recherche du Québec (FRQNT). M.F.-D. and F.X. acknowledge the partial support from the Government of Israel and Yale University. K.W. and T.T. acknowledge support from Japan Society for the Promotion of Science KAKENHI (grant nos 19H05790, 20H00354 and 21H05233).

## Author contributions

M.F.-D. conceived and carried out the experiments and simulations. M.F.-D. and F.X. analysed the results and wrote the manuscript. K.W. and T.T. synthesized the hBN crystals.

## Competing interests

The authors declare no competing interests.

## Additional information

**Supplementary information** The online version contains supplementary material available at <https://doi.org/10.1038/s41563-023-01596-z>.

**Correspondence and requests for materials** should be addressed to Matthieu Fortin-Deschênes or Fengnian Xia.

**Peer review information** *Nature Materials* thanks Lain-Jong Li, David Geohegan and the other, anonymous, reviewer(s) for their contribution to the peer review of this work.

**Reprints and permissions information** is available at [www.nature.com/reprints](http://www.nature.com/reprints).